Laser-Induced Heating in GdVO 4 : Yb 3+ /Er 3+ Nanocrystals for Thermometry

Yujiao Zhou, Gilles Ledoux, David Philippon, Sylvie Descartes, Matteo Martini, Shaozhou He, Cédric Desroches, Didier Fournier, Catherine Journet, Laurence Bois

Laser Induced Heating in $GdVO_4$: Yb^{3+}/Er^{3+} Nanocrystals for Thermometry

Yujiao Zhou[†,‡], Gilles Ledoux[§], David Philippon[‡,*], Sylvie Descartes[‡], Matteo Martini[§], Shaozhou He[‖], Cédric Desroches[†], Didier Fournier[⊥], Catherine Journet [†] and Laurence Bois[†,*]

[†] Laboratoire des Multimatériaux et Interfaces, UMR CNRS 5615, Univ Lyon, Université Claude Bernard Lyon 1, F-69622 Villeurbanne, France

[§] Institut Lumière Matière, UMR CNRS 5306, Univ. Lyon, Université Claude Bernard Lyon 1, F-69622 Villeurbanne, France

[‡] Laboratoire Lamcos, UMR CNRS 52589, Insa Lyon, Université Claude Bernard Lyon 1, F-69622 Villeurbanne, France

[⊥] UFR Faculté des Sciences, Univ. Lyon, Université Claude Bernard Lyon 1F-69622 Villeurbanne, France

[‖] Département génie électrique, Insa Lyon, Université Claude Bernard Lyon 1, F-69622 Villeurbanne, France

Supporting Information

KEYWORDS: upconversion fluorescence, laser heating, luminescence, optical thermometry, lanthanide.

ABSTRACT: Photoluminescent temperature sensors based on gadolinium orthovanadate ($GdVO_4$) doped with 10% ytterbium and 2% erbium, are developed and dispersed in different media (lubricant fluid, sol-gel glass and PDMS) to evaluate the best conditions for temperature measurement. Two excitation modes are considered: (i) visible excitation by a down-shifting (DS) process or (ii) NIR excitation by energy transfer upconversion (UC) between Yb and Er. The luminescence intensity ratio (LIR) of the thermally coupled Er^{3+} emission peaks varies linearly with temperature in the range of 25 - 300°C, and this variation is reversible. The impact of the laser power density on thermometry via UC process that has been verified with $GdVO_4$: Yb^{3+}/Er^{3+} powders and with its different dilutions (low and high concentration), shows that the LIR is highly dependent on the laser source intensity, the environmental temperature and the dispersed medium. When $GdVO_4$: Yb^{3+}/Er^{3+} powders are dispersed at high concentration, high laser power density leads to significant laser-induced thermal heating. However, at low concentration, this laser thermal effect is no longer influenced by the laser intensity. In this paper, we propose a method to directly measure the laser-induced heating temperature and to correct the error caused by this effect on temperature measurement. According to these results, $GdVO_4$: Yb^{3+}/Er^{3+} upconversion nanoparticles can be applied for temperature sensing even if the laser-induced thermal effect occurs in the system.

1. INTRODUCTION

The race to miniaturize mechanical, optical and electronic devices has become an inescapable trend over the past fifty years. The successful development of these new devices requires new and powerful techniques to characterize them.[1] One of the crucial parameters to characterize in miniaturized devices is temperature, and for this reason, nano-thermometry has been widely developed in the last decade.[2–5] Among the current methods for temperature sensing, luminescence thermometry is considered a promising method to reliably acquire temperature in a non-contact configuration with high sensitivity and accuracy.[2–9] These advantages have led to a wide range of applications in various fields such as micro/nano-electronics, integrated photonics,[6] biology for thermal therapies,[7,10] or more recently tribology for temperature measurement in a lubricated contact.[11,12]

By using the photoluminescent materials, we can use their emission intensity,[11,12] lifetime[13], spectral width, spectral shift, etc...[2] to measure the temperature. The method of ratiometric luminescence based on the Boltzmann distribution[14] is well known as a self-referenced measure:[2–9,15,16] the population of thermally coupled levels (TCLs) varies differently with temperature, and then the temperature dependence of the emission intensity ratio can be calibrated for use in thermometry.

For real-world applications, factors other than the luminescence of the material should be considered: the temperature range for adequate thermometry sensitivity, the physicochemical stability, availability and cost of the material. Lanthanide

ions (Ln^{3+}) can meet these requirements.[2,3,5,6,17] Doped into an inorganic crystalline host, Ln^{3+} ions emit sharp characteristic and strong peaks (*i.e.* TCLs transitions), which allow for high-precision ratiometric thermometry. To excite Ln^{3+} ions, several processes can be used: down-conversion using high-energy light;[18] up-conversion by multiple-photons,[19] FRET (Förster resonant energy transfer) process between two Ln^{3+} ions,[20] or even bimodal photon excitation coupling down & upconversion.[21] Different excitation processes can also interfere in the experimental temperature measurement by excitation regimes[22] and laser power density.[23] Several other factors can affect the thermometric accuracy, such as environmental conditions (pressure,[24] dispersion medium[25]) and intrinsic parameters including the nature of the lanthanide and the doped concentration,[17] the crystal quality,[26] the size of the nanoparticle (NPs),[27] the host compound.[28]

Er^{3+} was chosen as the temperature probe because of its specific temperature range (293 - 473 K) that matches our tribological application. The energy gap between Er^{3+} TCLs ($^4S_{3/2}$ and $^2H_{11/2}$ levels; ~ 700 cm^{-1}) allows for high thermometric sensitivity in this temperature range.[29–31] For example, in the Er^{3+} -coupled Yb^{3+} FRET system, the Yb^{3+} ion is used as a sensitizer to transfer energy to the Er^{3+}; this process is referred to ETU (energy transfer upconversion). In addition, the use of near-infrared (NIR) laser as the excitation source in an ETU system is very attractive for biological applications because of the high efficiency, and also because of the high spatial and temporal resolution thank to the large penetration depth of the NIR light.[32,33] However, several effects brought by the energy transfer process can interfere with the photoluminescent emission. For example, emission quenching due to the concentration of Ln,[34] the surface of the NPs,[35] the thermal effects[36] or the presence of OH,[37] can significantly reduce the intensity of the emission. Laser power density can also affect the intensity of the luminescence by interfering with the population of electrons in the excited state of the Ln ions.[38–41] In addition to radiative relaxations, some of the energy is converted to heat by non-radiative relaxation pathways.[42–45] In the upconversion process, the quantum yield is always low compared to other excitation processes because of the important non-radiative relaxation.[46] So, this heat can be significant and then affects the temperature measurement. In a non-linear optical process, the heating depends on the power density of the laser. Laser heating in β-$NaYF_4$:Yb^{3+}/Er^{3+} micro-powders at room temperature has been observed by Joseph *et al*.[39] for high laser power density (> 50 W/cm^2) as well as by Wang *et al*.[38] for lower laser power density (1-2.6 W/cm^2). Joseph. R. *et al* proposed a method to correct the induced variation of emission intensity.[39] The effect of laser power density on the photo-thermal conversion ability of $BiVO_4$, Yb^{3+}, Er^{3+} sample has been studied and the induced temperature increment increased monotonically with the laser power density.[44] The influence of the particle morphology on non-radiative process[47] was also studied: a higher non-radiative process associated with a higher red/green emission was evidenced in small nanoparticles. This laser heating effect could be beneficial because Ln^{3+} doped NPs are used as nano-heaters in the field of photothermal energy.[43–45,47] Precise and selective heating at the nanoscale could be applicated in cancer treatment, data storage[48–51] or microflow control.[52] The combination of optical heating and thermometry in Ln-doped materials was first studied by Wawrzynczyk *et al.,*[53] Debasu *et al.* [54] and Pinol *et al*.[55] Subsequently, many works have described that the erbium-containing particles could be used as both nanothermometers and optical heaters, in different hosts such as fluoride,[47,56,57] oxide,[43] molybdate,[58] tungstate,[59] phosphate,[59] or vanadate.[44,60,61] Continuous-wave excitation is commonly used, however non steady-state upconversion based on pulsed excitation allows to avoid undesired non-radiative energy transfer.[62–64] In addition to the laser heating, there are other laser-induced effects in Er^{3+} doped composites. An additional Er^{3+} transition ($^2H_{9/2} \rightarrow {}^4I_{13/2}$) has been observed under continuous-wave laser intensities above 10 W/cm^2.[65,66] This additional transition, which overlaps with the green emission ($^4S_{3/2} \rightarrow {}^4I_{15/2}$) that is normally used for thermometry, can lead to calibration errors in ratiometric thermometry which need to be carefully checked.

Here, our objective is to develop an upconversion (UC) photoluminescent thermometry sensor in nanoscale temperature measurement during tribological friction. The nano sensor is homogeneously dispersed in a medium (solid or fluid) chosen for the friction. To reduce the emission from the matrix, and to optimize the spatial resolution, the NIR laser excitation is chosen. However, the laser-induced heating effect is well known in UC process upon NIR continuous-wave laser, thus we focus on the adverse thermal effects of lasers on the ratiometric thermometry of Er^{3+} at down and upconversion luminescence. The laser heating phenomena in UC doped Ln^{3+} nanoparticles is first analyzed at different temperatures and then calibrated as a function of laser power density. We propose a method to calculate the temperature difference induced by the laser thermal effect, which can be used to rectify the error caused by laser heating using UC Ln^{3+} doped NPs. Secondly, we focus on the effects of laser heating on UCNPs dispersed in a medium, fluid or solid, to evaluate how does the heat dissipation influence the temperature calibration measurements. Vanadate hosts were chosen because of their high UC emission as well as laser induced-optical heating due to their high phonon frequencies.[67] The thermal effect of the laser on $GdVO_4$: Yb^{3+}/Er^{3+} NPs powder was studied with 488 nm and 970 nm excitation at different laser intensities and temperatures up to 300°C. $GdVO_4$: Yb^{3+}/Er^{3+} NPs were also dispersed in fluid and solid media at two NP concentrations. The experiments were performed under the non-saturation regime of the NIR laser in order to maintain the 2-photon ETU condition.

2. MATERIALS AND METHODS

2.1. Material.

The chemicals were used as follows: $Gd(NO_3)_3$ hydrated (Alfa Aesar 99.9%), $Yb(NO_3)_3$ hydrated (Sigma-Aldrich 99.9%), $Er(NO_3)_3$ hydrated (Alfa Aesar 99.9%), NH_4VO_3 (min. 99.0%, Alfa Aesar), NaOH (Sodium hydroxide pellets, min. 99%, MERCK). A conventional mono-pentaerythritol lubricating oil (Nycobase 5750, supplied by NYCO, Paris, France) was chosen as the solvent to study the effect of the environment on the thermometric performance of the probes. The solids were ob-

tained by soft chemistry processes using the chemicals: NPs $GdVO_4$: Yb^{3+}/Er^{3+} ground powder, MTEOS (Methyltriethoxysilane 98%, abcr), EtOH (Ethanol anhydrous, Carlo Erba Reagents), Hydrochloric acid (HCl 37%, Carlo Erba Reagents), 3-aminopropyltrimethoxysilane (APTES, 95%, ACROS Organics), SYLGARD® 184 Silicone Elastomer (PDMS Polydimethylsiloxane, DOW).

Synthesis of $GdVO_4$: Yb^{3+}/Er^{3+} NPs. A chemical co-precipitation technique was used to prepare $GdVO_4$: 10% Yb^{3+}; 2%Er^{3+} nanoparticles.[1,2,68] Solution 1: 0.05 M $NaVO_3$ aqueous solution at pH 12, prepared by adding NH_4VO_3 in 0.15 M NaOH solution; Solution 2: Solutions in distilled water of 0.05 M $Ln(NO_3)_3$ in stoichiometric ratio (Gd^{3+}: 88% mol.; Yb^{3+}: 10% mol.; Er^{3+}: 2% mol.). Solution 2 was slowly added to solution 1 (dropwise), the mixture became turbid with a white precipitate. After heating under stirring at 60°C for 1 h, the precipitate was separated by centrifugation, and washed with distilled water for 3 times. The powder was dried at 80°C in an oven overnight and then annealed in air at 600°C for 2 h.

Preparation of a suspension of $GdVO_4$: Yb^{3+}/Er^{3+} in a lubricant. The suspension of $GdVO_4$: Yb^{3+}/Er^{3+} nanoparticles was prepared by adding the ground powder in an ester-based oil (Nycobase 5750) at mass concentrations of 0.5 wt.% or 50 wt.%, followed by mechanical stirring and by ultrason at room temperature for 30 minutes, respectively.

Solid preparation of $GdVO_4$: Yb^{3+}/Er^{3+} in a hybrid glass or PDMS polymer: In Glass: 5 wt.% of NPs. The NPs hybrid glass was prepared by a sol-gel procedure via hydrolysis and condensation of the MTEOS precursor in acid water (HCl pH =2.4, 1:0.3 by mass) and ethanol (1:0.8 by mass).[69] After 18 h of stirring at room temperature, the solvent was removed by evaporation under vacuum. A quantity of NPs powder was then dispersed in the concentrated sol and stirred ultrasonically for 10 minutes. To accelerate condensation, 2 vol.% of APTES was added to the mixture under stirring. Then, the NPs suspension in the sol was placed in an oven at 50°C for gelation and subsequent drying to a solid glass. In our case, 5 wt.% of NPs powder in the sol is the maximum amount that can be dispersed to obtain a transparent glass.

In PDMS: 5 wt.%; 50 wt.% of NPs. PDMS polymer with 5 wt.% or 50 wt.% NPs was prepared by polymerization at room temperature. The NPs powder was first mixed with the PDMS silicone precursor under mechanical stirring, the initiator (1:10) was added to start the polymerization.

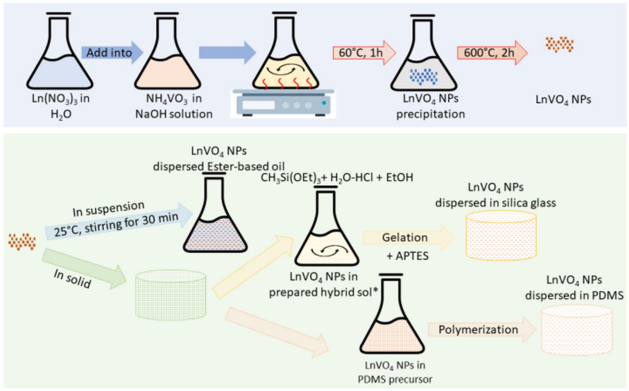

Scheme 1: Overview of the process used for the preparation of the materials. *Prepared hybrid sol: Hybrid silica sol after hydrolysis, condensation, and evaporation process.

2.2. Characterizations.

The crystalline phase of the synthesized nanoparticles was characterized by an X-ray diffractometer (Bruker D8 Advance diffractometer) with Cu Kα radiation (λ = 1.54060 Å) operating at 45 kV and 30 mA at room temperature. Diffractograms were collected at 2θ between 5 and 70° with steps of 0.016°. The morphology of the nanoparticles was analyzed by transmission electron microscopy (TEM, JEOL 2100F 200 kV). Scanning electron microscopy SEM images were obtained using a Zeiss Merlin Compact SEM with a secondary electron detector at a low accelerating voltage up to 5 kV. The backscattered electron detector (BSD) was used at 20 kV. Dynamic Light Scattering (DLS, Malvern-Zetasizer) was used to analyze the NPs suspension.

The upconversion emission studies were performed on a modular spectrofluorometer, equipped with different laser excitation sources, a temperature controller (LINKAM Optical DSC600 cell), a detector (CCD, Short Focal Length Triple Grating Imaging Spectrographs, TRIAX 320 HORIBA) with an optical fiber. The lasers used in this work were, respectively, a continuous-wave NIR laser (970 nm, MDL-2W) focused on the sample to a spot size of 4 mm^2 and an unfocused pulsed OPO UV-visible laser (488 nm, EKSPLA NT230-50-SH, 10 mJ pulsed energy). During the temperature calibrations, powder and solid samples were placed directly on a piece of silicon in air, while fluid samples were poured into a sapphire bowl closed with a glass lid. Data was collected 10 s after the stabilization of temperature and laser.

Absorption spectra of the powders were performed with a LAMBDA 365 UV/Vis (Perkin Elmer) Spectrophotometer in the wavelength range 350 - 1100 nm and with an integrating sphere for solid samples. Transmission spectra were analyzed by LAMBDA 900 (Perkin Elmer) Spectrophotometer in the wavelength range 350 - 2500 nm for transparent samples.

Thermal conductivity was studied using MTPS (Modified Transient Plane Source) with a TCi thermal conductivity analyzer (C-Therm, TCi-3-A).

2.3. Data analysis.

The thermometry of Er^{3+} doped materials has been analyzed by LIR theory. The population ratio on two thermally coupled energy levels (N_{L2} and N_{L1}) varies with temperature according to equation (1). As the population of the energy level (N) is directly proportional to the emitted intensities (I), the LIR also follows the Boltzmann distribution.

$$LIR = \frac{N_{L2}}{NL_1} = \frac{I_{L2}}{I_{L1}} = \frac{g_2\sigma_2\omega_2}{g_1\sigma_1\omega_1} exp(-\frac{(E_2 - E_1)}{k_B T}) = B\ exp(-\frac{\Delta E}{k_B T})$$

(1)

The emission band areas of the were integrated by using Simpson's rule to calculate the average of the total emitted intensities for each transition.[70] The Er^{3+} emission spectra was collected and then analyzed by MATLAB software. The integrated area ranges were 540 - 567 nm (L_1: $^4S_{3/2}$ to $^4I_{15/2}$) and 512 - 540 nm (L_2: $^2H_{11/2}$ to $^4I_{15/2}$) as Figure S1 shows. The LIRs of the Er^{3+} peaks (L_1 and L_2) were processed with Excel software for plotting and data analysis. The intrinsic experimental uncertainty on emission intensity (δI/I) depended on the detector, is mainly determined by the signal-to-noise ratio (SNR)[71] (equation S1, Supporting information). In the Boltzmann equation (1), N_i denotes the population of excited ions, and I_i is the emitted intensity for a given level *i*. The pre-exponential constant B includes the g_i , σ_i , ω_i, which are the degeneracy, the emission cross section, and the angular frequency of transitions for a given level *i*, respectively. ΔE is the energy gap between the two thermally coupled energy levels, k is the Boltzmann constant, and T is the absolute temperature.[14] ΔE can be determined by the calibration curve of Ln(LIR) versus 1/T. Compared to the theoretical value, this experimental value can be used to check the accuracy of the temperature value. In addition, the relative thermal sensitivity S_R, defined by equation (2), is also an important indicator of the measurement reliability.[72]

$$S_R = \frac{1}{LIR} \times \frac{d(LIR)}{dT} = \frac{\Delta E}{k_B T^2}$$

(2)

3. RESULTS AND DISCUSSIONS

This section will be divided into two parts. The first part will deal with the characterization of the free $GdVO_4$: Yb^{3+}/Er^{3+} powder while the second part will consider the nanoparticles dispersed in a matrix. This matrix will be fluid (ester-based oil) or solid (PDMS or Hybrid glass).

3.1. Free powder: Nanoparticles {$GdVO_4$: Yb^{3+}/Er^{3+}}

Structural characterizations. The XRD pattern of the synthesized $GdVO_4$: Yb^{3+}/Er^{3+} (Figure 1a) matches well with the theoretical planes of the tetragonal phase (JCPDS 17-0260). The product consists of pure gadolinium vanadate with space group $I4_1/amd$. SEM and TEM images (Figure 1b and 1c) show that the nanoparticles are elongated ellipsoidal crystallites with the lengths of 30 nm and their formed clusters is at the length 300 nm.[73] This size of aggregation is not a problem for our application, but solutions could be considered to limit it.[74–76] The HRTEM image (Figure 1d) shows a well-defined crystal structure with a lattice fringe distance of 0.27 nm and 0.47 nm which corresponds to the (112) and (101) interplanar spacing of $GdVO_4$ respectively (JCPDS 17-0260). A porous cell-like nanostructure can also be observed,[77] these voids are the result of high temperature atomic diffusion.[73]

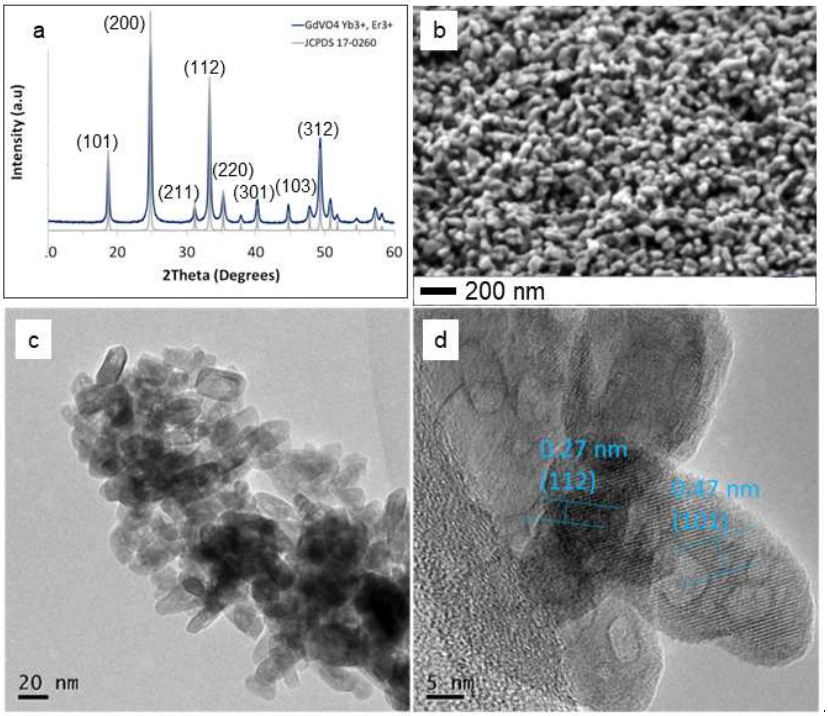

Figure 1: (a) X-ray diffraction pattern. (b) SEM; (c) TEM and (d) HRTEM images of the $GdVO_4$: Yb^{3+}/Er^{3+} powder sample.

Optical characterizations: photoluminescent properties. In Figure 2a, the blue line shows the absorption spectrum of $GdVO_4$: Yb^{3+}/Er^{3+} NPs in the wavelength range of 350–1100 nm. $GdVO_4$: Yb^{3+}/Er^{3+} NPs absorb NIR light (985 nm) and some visible light. The green lines represent the emission spectra of $GdVO_4$: Yb^{3+}/Er^{3+} (solid line: under a 970 nm laser at 2.5 W/cm^2, dashed line: under a 488 nm laser at 50 mW/cm^2). Both spectra show strong bands in the green region, and some weak bands in the red emission region.[73,79,80] Comparing these emission spectra, the main Er^{3+} transitions appear under both excitations (970 nm or 488 nm): 525, 555 and 665 nm corresponding to $^2H_{11/2}$, $^4S_{3/2}$ and $^4F_{9/2}$ to the ground state respectively. Moreover, the transition from $^2H_{9/2}$ to $^4I_{13/2}$ has not been observed.

As shown in Figure 2b, these two excitation mechanisms are different. Under the excitation by a 488 nm laser, Er^{3+} electrons are promoted to the $^4F_{7/2}$ state, and then decay into the emitting states by non-radiative relaxation, called down-shifting (DS). Conversely, by exciting at 970 nm, Er^{3+} can be excited by two-sequentially absorbed photons (Ground-state absorption (GSA) and excited-state absorption (ESA), respectively shown in the black arrow)[18] to the $^4F_{7/2}$ excited state and generates the same emissions,[44,81–83] this process was afterward verified in our experiments. However, since the absorption effective cross section of Yb^{3+} in the NIR region ($^2F_{7/2}$ to $^2F_{5/2}$) is much larger than that of Er^{3+} ($^2I_{15/2}$ to $^4I_{11/2}$), the energy transfer between Yb^{3+} and Er^{3+} (the ETU process) will be the most important process.[68] It can also be noted that the existence of other cross-relaxations and of some energy back transfer (EBT) from erbium to ytterbium (Figure 2b).[44,78,84,85] In both excitation processes, the non-radiative relaxations are larger in the UC process than in the DS process, *i.e.* the quantum yield is lower. In the studied temperature range, the population of the $^2H_{11/2}$ state increases while the $^4S_{3/2}$ state decreases with increasing temperature according to the Boltzmann distribution,[4,80] as shown in Figure 2c.

Thermometry by the LIR method: effect of laser intensity. As mentioned above (Figure 2c), the influence of temperature on the photoluminescent spectra of $GdVO_4$: Yb^{3+}/Er^{3+} NPs has been verified. Assuming that the laser can induce heating, the temperature measurement should necessarily be affected. When excited by an unfocused 488 nm laser, two laser power densities are used: approximately at 50 mW/cm^2 as the maximum density and at 5 mW/cm^2 as the reduced density. For excitation by a 970 nm laser, eight different laser power densities are applied, ranging from 0.3 W/cm^2 to 15.8 W/cm^2. Under NIR excitation, the luminescent signals at 0.3 W/cm^2 are too weak to be analyzed, so the temperature calibration was started at 1.3 W/cm^2. Under these conditions, we avoid saturation of the intermediate upconversion levels, and the thermometry will only work in a unsaturated excitation regime.[22]

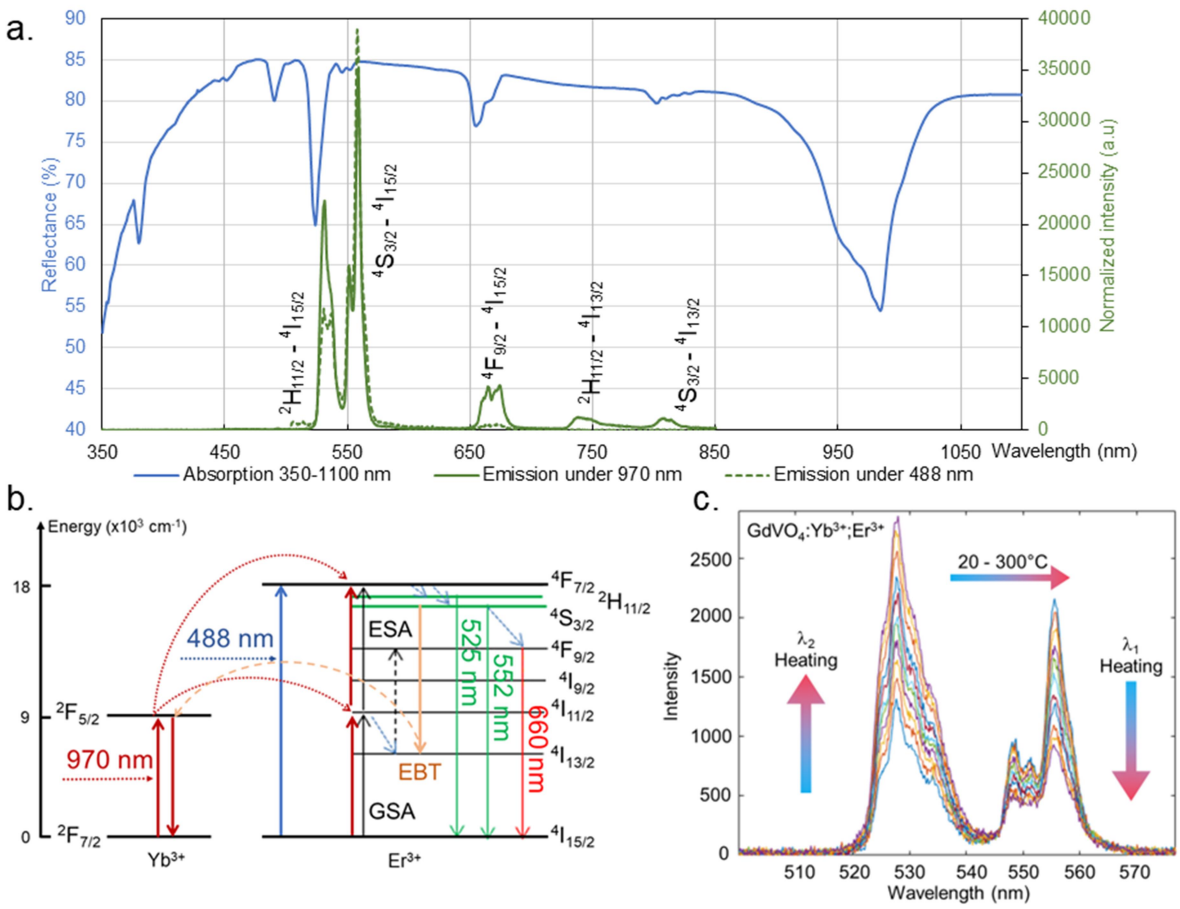

Figure 2: (a) Absorption spectrum (350 – 1100 nm) of $GdVO_4$: Yb^{3+}/Er^{3+} powder sample in blue line, emission spectra of $GdVO_4$: Yb^{3+}/Er^{3+} powder sample in green lines (solid line: under 970 nm laser; dashed line: under 488 nm laser). (b) Er^{3+} and Yb^{3+} simplified energy-level diagram, showing the main energy transfers (more energy transfers have been studied in Liu's *et al.* works[78]) the possible emission mechanism under 970 nm (red arrow) and 488 nm (blue arrow) excitations, respectively. (c) Emission spectra at different temperatures of the $GdVO_4$: Yb^{3+}/Er^{3+} powder sample (under 970 nm laser at 2.5W/cm^2), showing the thermally coupled levels λ_1 and λ_2.

Figure 3 shows the emission spectra at 20°C via DS (Figure 3a) and UC (Figure3b). The emission intensity increases as the laser power density increases, which is related to the increase in the electron population in the excited state of Er^{3+}. There is no emergence of a new peak at high laser power density; in particular, the $^2H_{9/2} \rightarrow {}^4I_{13/2}$ intruding emission from Er^{3+} was absent in the studied laser power density range. This phenomenon was considered as an important interference for the calculation of LIR.[65,66,86] In addition, it should be noted that the resolution is different between the two excitation conditions due to the different detector configuration, and the different range of laser intensities.

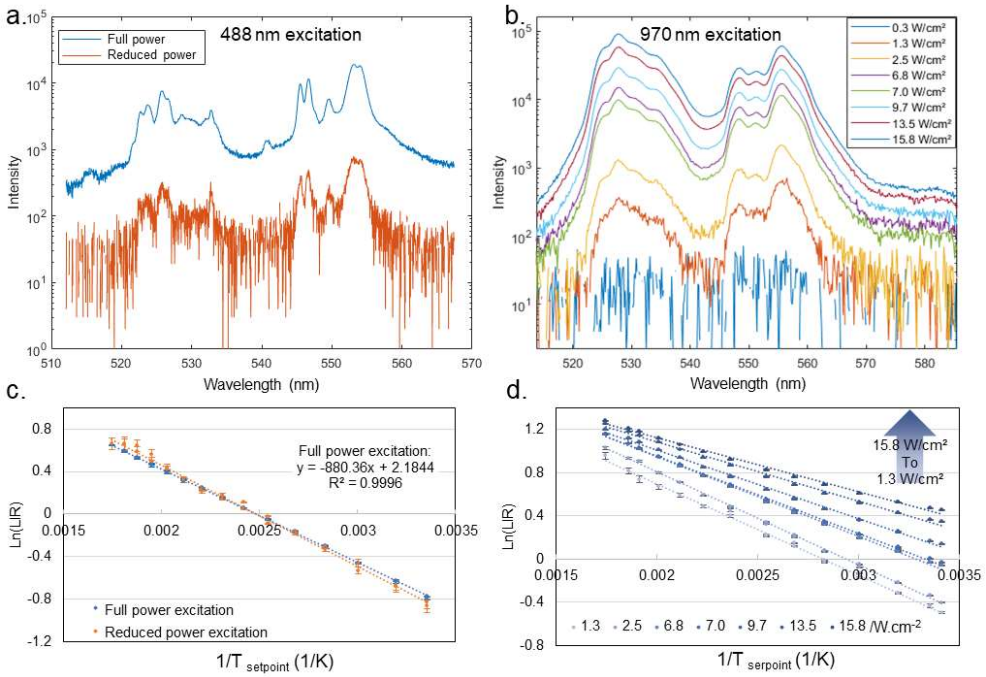

Figure 3: (a) Emission spectra of the $GdVO_4$: Yb^{3+}/Er^{3+} powder sample under excitation at 488 nm at full laser power density and at reduced laser power density. (b) Emission spectra of the $GdVO_4$: Yb^{3+}/Er^{3+} powder sample under excitation at 970 nm at 8 different laser intensities (0.3–15.8 W/cm^2). (c) Temperature calibration under excitation at 488 nm at two laser intensities. (d) Temperature calibration under excitation at 970 nm at different laser intensities.

In Figures 3c and 3d, Ln(LIR) is plotted as a function of the setpoint temperature (named $T_{setpoint}$), each calibration curve is linear and reversible in the temperature range studied (20 – 300°C). It is observed that the calibration curves overlap in the DS system (Figure 3c), while the intrinsic uncertainty of the curve at reduced laser intensity was relatively large. It's important to note that the reliability of the temperature calibration may depend on the uncertainty, calibration at full laser power excitation should be more reliable. On the other hand, the temperature calibration curves for the UC process change with laser intensity, and the uncertainty decreases when laser intensity increases. (Figure 3d). As expected, the laser power density influences the ratiometric thermometry in the UC system but not in the DS system. The slope of the calibration curves can be used to calculate the inferred energy difference (ΔE_{LIR}) using the Boltzmann equation (equation (1)), and the ΔE_{LIR} is considered as an indicator of the reliability of the temperature measurement.[72] Indeed, if no laser effect occurs, the value of ΔE should remain constant. In Table 1, the ΔE_{LIR} calculated by the slope of temperature calibration curves via DS excitation indeed remains constant when the laser power density changes, whereas the ΔE_{LIR} of the UC system decreases as the laser power density increases. The ΔE_{LIR} values and the pre-exponential constant B were plotted as a function of the laser intensity in Figure 4a. Since laser power density does not influence either the ratiometric thermometry or the pre-exponential constant, for further comparison, the ΔE_{LIR} and B, calculated by DS at 50 mW/cm^2, were set to 0 W/cm^2 (Figure 4a). Note that the ΔE_{LIR} for low NIR laser intensities is similar to the ΔE_{LIR} of the DS system. For high NIR laser intensities, it decreases when the laser power density increases. The B value decreases as the laser density increases and it is explained by the fact that non-radiative process increases.[18] The relative sensitivities were calculated by using equation (2), and it decreases with increasing laser intensity (Figure 4b). It is assumed that this decrease is actually caused by an increase in temperature.[68]

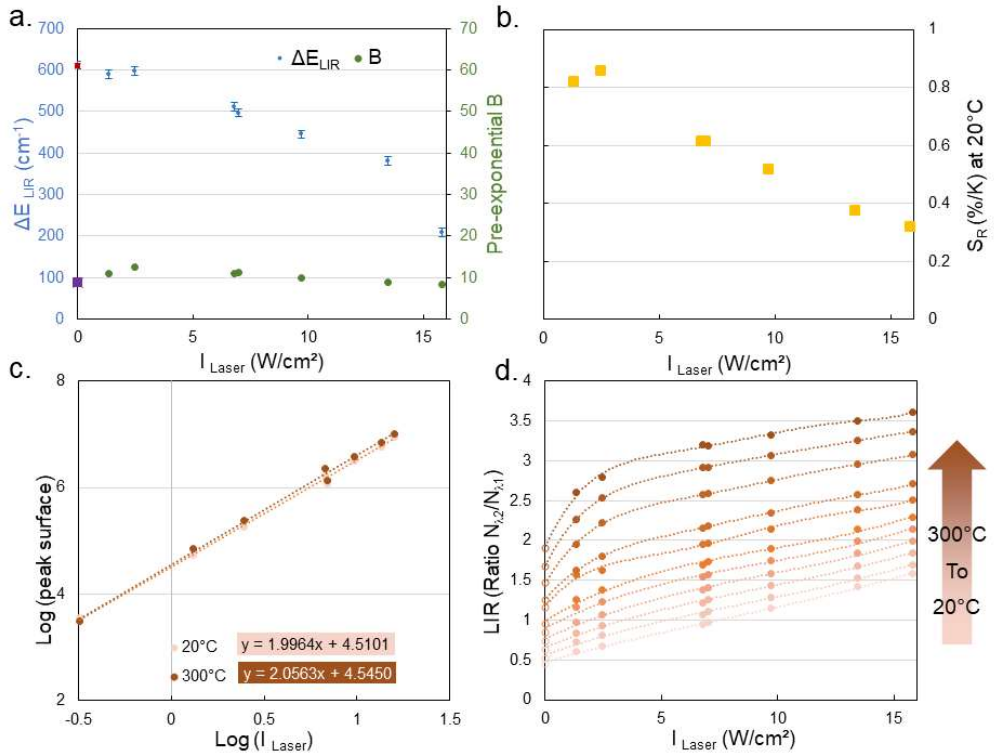

Figure 4: (a) Energy gap ΔE_{LIR} (blue marks) and pre-exponential constant B (green marks) calculated from the calibration curves for each laser power density (DS series in square marks (red and purple, respectively) at 0 W/cm^2 for comparison). (b) Relative sensitivity S_R at 20°C (setpoint temperature) for each laser intensity. (c) Relationship between the sum of λ_1+λ_2 surface peaks and the laser intensity at 20°C and 300°C. (d) LIR at different laser intensities from 20°C to 300 °C under NIR laser, in comparison with the DS process (50 mW/cm^2 of 488 nm laser excitation) shown by the hollow dots.

Table 1. Calculated energy gaps ΔE_{LIR} from calibration curve

Excitation§	**488 nm**		**970 nm**												
I_{Laser} (W/cm^2)	50.10^{-3}	5.10^{-3}	1.3	2.5	6.8	7.0	9.7	13.5	15.8	9.7	13.5	15.8	9.7	13.5	15.8
Media	Powder									0.5 wt.% in suspension			5 wt.% in glass		
Slope¤	-880	-955	-848	-859	-737	-715	-641	-549	-301	-894	-924	-890	-771	-767	-789
B	9	11	11	12	11	11	10	9	8	11	12	11	7	7	8
ΔE_{LIR} (cm^{-1})	612	663	589	597	512	497	445	382	209	622	642	618	536	533	548
Uncertainty (%)	2.7	16.1	6.1	1.9	0.5	0.4	0.3	0.3	0.3	30.3	20.0	19.2	35.4	14.8	10.4

§Excitation under 488 nm pulsed laser, or under 970 nm continuous laser.

¤Slopes of the calibration curves, ΔE (energy gap determined by linear regression in Figures 3c, 3d, 7a and 7b) and B (pre-exponential constant calculated by the curves) for each temperature calibration curve (equation (1)).

Laser heating via UC. In two photons systems, the excited population increases quadratically with the laser power density. The sum of peak surface S1 (peak N1: 540 to 560 nm) and S2 (peak N2: 520 to 540 nm) is integrated (Figure S1) and plotted as a function of the laser intensity (Figure 4c). The slopes are around 2 at extreme temperatures (20°C and 300°C). Such behavior is a crucial indication that the excitation system is always a 2-photons system in the studied temperature range. Since the doped concentration of Er^{3+} is relatively low (2 mol. %), the ETU process from Yb^{3+} to Er^{3+} should be the most important mechanism under our conditions. Furthermore, no new transition has been observed in the emission spectra and the calibration curve is always linear up to the maximum laser power density studied, the non-saturation regime of the excitation was also verified. Thus, the LIR value can only be affected by the temperature variation.

The chart of LIR versus laser intensity at different temperatures (Figure 4d), shows that the LIR values change not only with the temperature but also with the laser intensity. The series of total laser power density per DS excitation are represented by the hollow markers at 0 W/cm^2 in the chart. The laser intensity does not change the temperature calibration in DS system, *i.e.,* in the case of temperature calibration at 488 nm, regardless of the laser power density, the equation of the curve corresponds to the Boltzmann distribution (equation (1)). On the other hand, the LIR value under UC excitation increases with the laser intensity for a given temperature. As the LIR value is directly proportional to the temperature, it can be assumed that the temperature increases with the laser intensity; the NIR laser heats the sample during the temperature calibration measurements. It should be also noted that the induced heating phenomena highly depends on the sensitizer content used.[42,44,87,88]

Self-calibration/correction of laser heating. As shown previously in Figure 3c, the laser heating is negligible in the DS system, the temperature calibration under 488 nm laser at 50 mW/cm^2 can therefore be considered as a correct distribution corresponding to Boltzmann's law (equation (1)). This equation (3) can be translated by using a linear regression on the curve in Figure 3c, and is used in the following as a reference.

$$Ln(LIR) = 2.1844 + \frac{(-880.36)}{T_{LIR}}$$

(3)

Equation (3) is then used to estimate the temperature of the sample measured by LIR values (named T_{LIR}) for various laser intensities and temperature setpoints for UC system. Considering that only laser heating occurs in the previous experiments, it is therefore possible to calculate the temperature change due to the contribution of the laser heating (named δT) and set by the temperature controller as follows:

$$\delta T = T_{LIR} - T_{setpoint}$$

(4)

These values were, as expected, positive because the measured temperatures (T_{LIR}) were higher than the setpoint temperatures ($T_{setpoint}$) during the calibration. δT is plotted as a function of $T_{setpoint}$ for different laser intensities (I_{laser}) in Figure 5a for all LIR data collected during the temperature calibration under NIR excitation. It varies with I_{laser} and $T_{setpoint}$. $T_{setpoint}$ interferes slightly with δT and this influence becomes more important as $T_{setpoint}$ increases. The low laser intensity series (1.3 W/cm^2 with hollow points) shows more fluctuations than the others because of its relatively important uncertainty, so they were not taken in calculation of laser heating correction. The curves of δT versus I_{laser} for each $T_{setpoint}$ (20 - 300°C) are plotted in Figure 5b. It can be observed that δT is linearly proportional to I_{laser} when $T_{setpoint}$ is below 150°C. For a $T_{setpoint}$ above 150°C, linearity is only respected when the laser intensity is higher than 5 W/cm^2. All slopes of curves are almost equal, however the intercepts increase with $T_{setpoint}$.

Assuming that the δT is totally caused by laser-induced heating, the relation between δT and $T_{setpoint}$ is consistent with the literature:[89] the thermal effect of laser becomes more important with increasing temperature, which has been explained by the fact that the relaxation rate of the multiphonon increases with temperature, and thus the thermal effect of the laser becomes more important at high temperature. Furthermore, the linearity of δT as a function of I_{laser} is also consistent with Sun's *et al*. results which show linearity between the laser induced heating and the laser power density used at room temperature.[44] The direct proportion between the δT and the $I_{laser\ heating}$ respects the fact that in the non-linear optics, the laser-induced heat increases as the laser intensity increases.

The above information shows that the laser-induced heating temperature is affected by the laser intensity. In order to correct the laser-induced heating temperature in thermometric calibration, all the data collected from 20°C to 300°C for the laser intensity of 2.5-15.8 W/cm^2 were fitted by a polynomial regression model with multiple predictors (here I_{laser} and T_{LIR}) and cross terms (here $I_{laser}.T_{LIR}$) according to the following equation:

$$T_{corrected} = C1 + C2 * I_{laser} + C3 * T_{LIR} + C4 * I_{laser}^2 + C5 * T_{LIR}^2 + C6 * I_{laser} * T_{LIR}$$

(5)

where $T_{corrected}$ is the corrected temperature at a given laser intensity and for a given measured temperature (T_{LIR} from LIR equation (3)). $T_{corrected}$ were plotted according to the equation (5) (with constant values (C1-C5) gathered in SI Table S2) in Figure 5c. The Figure 5c shows that the corrected temperatures values (line) are in good agreement with the setpoint temperature (symbols), with less than 5% of error. This observation confirms that the proposed model is well adapted for the correction of the laser heating temperature. This result is corroborated by Figure 5d where $T_{corrected}$ is drawn as a function of $T_{setpoint}$ and where all the data collapse on the line. It's important to note that this calibration equation (5) could be applied for any correction of laser-induced heating, but the constant values could vary slightly depending on the experimental conditions, such as the optical performance of the thermosensor or the dispersed media (Figure S5d).

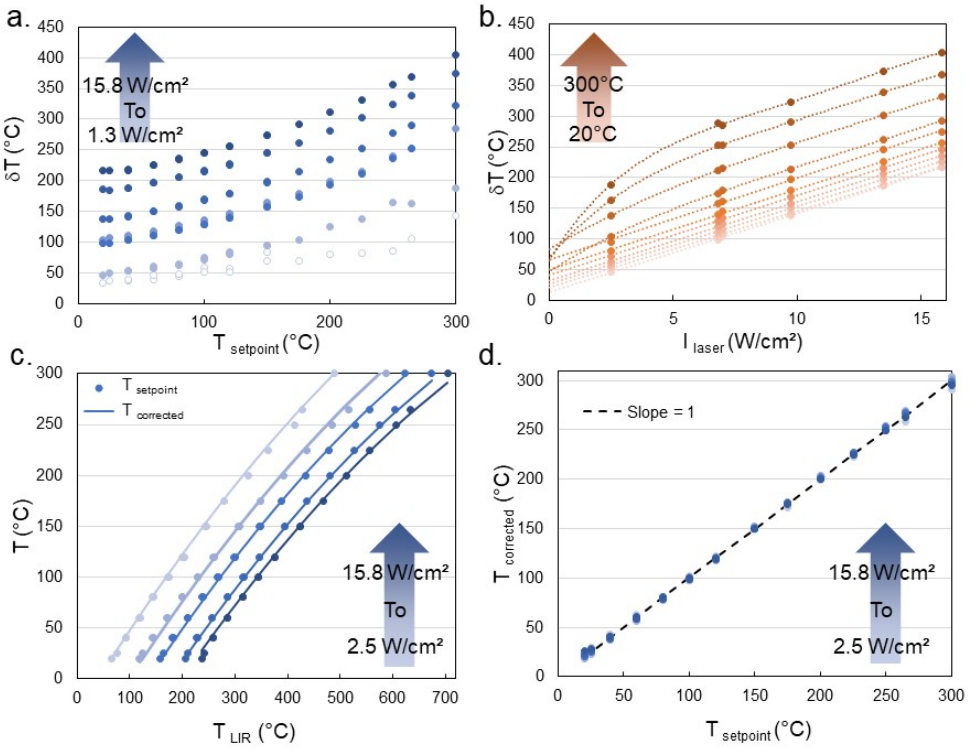

Figure 5: (a) Estimated temperature induced by laser heating at different laser intensities (1.3 – 15.8 W/cm^2) for regulated temperature from 20°C to 300 °C. (b) Effect of temperature on the estimated temperature of laser heating at different laser intensities. (c) Corrected temperature ($T_{corrected}$) (line) at different estimated temperature (T_{LIR}) compared with setpoint temperature (point). (d) Application of correction module for laser heating temperature.

The previous observations show a great interest for the thermometry application of $GdVO_4$: Yb^{3+}/Er^{3+} nanoparticles. Indeed, the calibration of the laser heating becomes possible to correct the laser-induced error, and then to precisely calibrate the $GdVO_4$: Yb^{3+}/Er^{3+} nanoprobes in thermometry measurements. Knowing that the laser-induced thermal effect occurs even at low NIR laser intensity and this effect rises with environmental temperature, the correction of the laser heating is necessary for upconversion probes to avoid any error in the temperature measurement. In addition, this laser-induced heating temperature calibration method could also be used for some applications, where upconversion NPs can be both the heater and the temperature sensor. Attention should be paid to the structural change of the material caused by high laser-induced heating temperature, it could reach 700°C upon laser intensity of 15.8 W/cm^2 and at environmental temperature of 300°C. The $GdVO_4$ nanoparticles have been observed by Gavrilović *et al.*[90] that after calcination of 2 h at 800°C, their size has slightly increased, and their crystal phase has not changed. Therefore, we do not expect for any structural transformation of the nanoparticle under short time excitation by NIR laser. However, this temperature could cause irreversible structural change in other nanoparticles.

3.2. Suspension & Solid with nanoparticles $GdVO_4$: Yb^{3+}/Er^{3+}.

The results in the previous section were obtained from $GdVO_4$: Yb^{3+}/Er^{3+} nanoparticles powder. The laser heating effect was observed in the NPs powder via the UC process, and may be negligible at low laser intensity. For applications as temperature sensors, the NPs must be included with a certain concentration in a given medium. Environmental conditions, such as, the chemical or physical impact of the medium, the concentration of the nanoprobes, the optical compatibility of the medium…can be critical for obtaining correct temperature measurement results.[7] In the following, in order to determine the impact of environmental factors on temperature calibration (including laser-induced heating), the $GdVO_4$: Yb^{3+}/Er^{3+} nanoprobes were dispersed in three different media, one liquid and two solids, at different concentrations. The mixtures were excited by a NIR laser at different intensities for temperature calibration.

Matrix characterizations. An ester-based oil (Nycobase 5750) was chosen as a fluid medium to apply $GdVO_4$: Yb^{3+}/Er^{3+} nanoprobes for tribological temperature measurement.[12] Nycobase oil is used as a basic lubricant because of its properties: rheological, high thermal resistance, chemical stability, non-toxicity. The nanoprobes can also be dispersed in solid media to explore their potential application in optical thermometry for local temperature measurement, such as measuring the local temperature of the near-surface layer of a solid in tribology. Therefore, hybrid glass and PDMS were chosen as solid matrices. As shown in Figure 6a, the absorbance in the NIR wavelength range of the pure matrices, oil

(Nycobase), hybrid glass and PDMS is almost zero. Therefore, they cannot be heated by the NIR laser. They all have very low thermal conductivity (Table S1). The heat dissipation can be neglected in these matrices.

After the homogenous dispersion of NPs in the fluid medium, the aggregation state of NPs in oil is determined by DLS. The hydrodynamic size of the nanoparticle agglomerate in the 0.5 wt.% NPs suspension is about 400 nm (Figure 6b). The dispersion in the solid (hybrid glass) was observed by SEM. Figure 6c shows a cross-sectional view of a hybrid glass slice in which 5 wt.% NPs were inserted by the sol-gel process. The white dots (< 5 µm) are the aggregates of $GdVO_4$ NPs. The aspects of the NPs/matrix mixtures are shown in Figure 6 (d1: oil suspension, d2: Silica glass, d3: PDMS), they became white with some transparency after dispersion of the NPs.

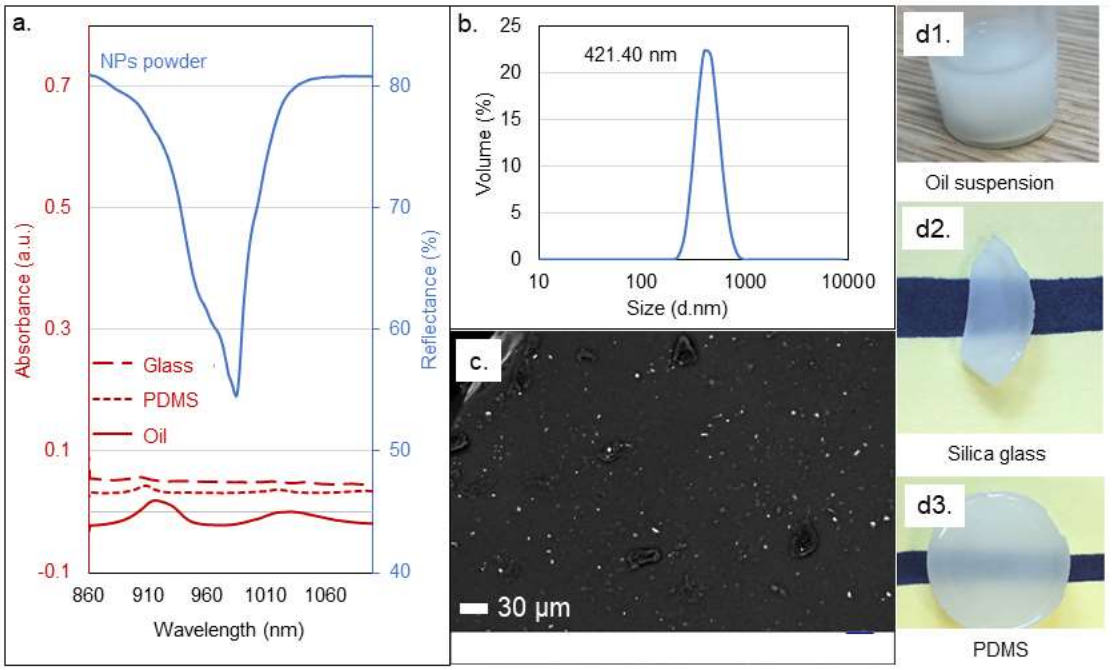

Figure 6: (a) Absorbance spectra for the pure matrix (oil, glass, PDMS) and reflectance spectra for the NPs powder. (b) DLS analysis of 0.5 wt.% NPs in suspension. (c) Backscattered electrons SEM image of the cross-sectional view of the hybrid glass containing NPs (5 wt.%). Photographs of the material prepared with 0.5 wt.% NPs. in suspension (d1); 5 wt.% NPs in hybrid glass (d2) and in PDMS (d3).

Dispersion in a fluid medium at low concentration. A low concentration suspension in oil at 0.5 wt.% of NPs was prepared. The emission intensity is low due to the low concentration of the luminescent probe in the suspension (Figure S2a), so the experimental uncertainty is quite large despite the relatively high laser power density used. As with the NPs powder, the emission intensity increases as the laser intensity increases, and the uncertainty becomes lower with higher laser intensity. However, the temperature calibrations curves (Figure 7a) from 25°C to 150°C, are all superimposed at various laser intensity (9.7 to 15.8 W/cm^2). As in Figure 4c, the integrated peak surface of S1 and S2 is plotted as a function of laser intensity for the NPs suspension (Figure S2b). A linear relationship with a slope of the curve close to 2 was observed, which is very similar to the case of free NPs powder (Figure 4c) which means that the excitation process is a UC involving two-photons absorption. The LIR values only change with temperature but not with laser intensity (Figure S2c), and the calculated energy gap (ΔE_{LIR}) are similar at different laser intensities (Table 1). Laser-induced heating is not observed in the 0.5 wt.% suspension of NPs in oil.

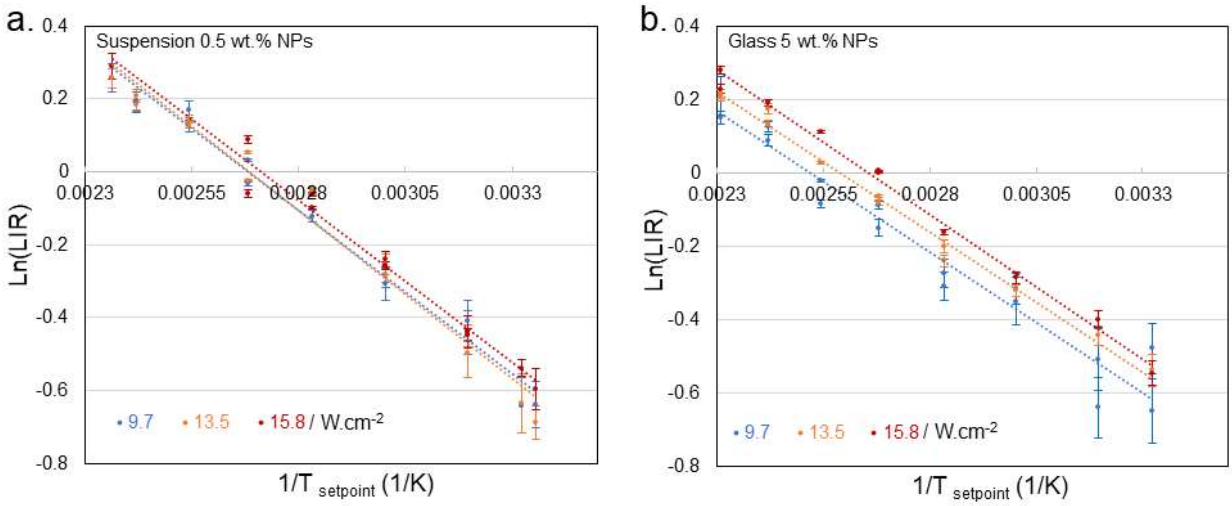

Figure 7: (a) Temperature calibration of the suspension at 0.5 wt.% NPs. (b) Temperature calibration of the glass at 5 wt.% NPs.

Dispersion in a solid medium at low concentration. Considering the dispersion capacity of NPs in the hybrid glass and PDMS, we used 5 wt. % of NPs to increase the emission intensity. The luminescence spectra of NPs dispersed in the hybrid glass are shown in Figure S3a. The emission spectra are noisy, and the experimental uncertainty is relatively high. In the temperature range from 25°C to 160°C, the temperature calibration curves do not change and the slope remains constant as the laser intensity varies (Figure 7b & Table 1). Excitation is always a UC process with two-photons absorption for all temperatures and laser intensities (Figure S3b), and the LIR is held constant at constant temperature (Figure S3c). A simple comparison with 5 wt.% NPs in PDMS is performed for two laser intensities (6.8 and 15.8 W/cm^2) at 25°C. The LIR value does not change with the laser intensity. The previous results are confirmed by the calculated ΔE_{LIR} values (Table 1) for the 5 wt.% NPs in the hybrid glass: ΔE remains constant as the laser intensity changes. Compared to other calibrations without laser heating effect, like the calibration of 0.5 wt.% NPs suspension in oil and that of NPs powder under low laser intensity (≥ 2.5 W/ cm^2), the calibration of 5 wt. % NPs in solid shows a lower ΔE value. We assume that this difference is caused by the slight laser-induced heating in the solid. However, this heating did not change under different laser intensities up to 15.8 W/cm^2. We can conclude that the calibration curves were not interfered by the excitation laser intensity in the 5 wt.% NPs hybrid glass or PDMS in the temperature range [25°C – 160°C] and laser intensity range [9.7 – 15.8 W/cm^2].

Dispersion in a medium at high concentration. In the previous section, it was observed that for a low concentration dispersion of NPs in a medium, solid or fluid, the influence of the excitation laser intensity can be neglected. However, a decreasing concentration of NPs degrades the signal-to-noise ratio of the emission spectrum, then the experimental accuracy. For our further study on temperature measurement under tribological conditions, we need to increase the probe concentration for the best accuracy of measurement without being perturbed by laser-induced heating problems. Therefore, a high concentration may be a good choice to optimize the quality of the emission spectrum. In this case, the effect of NPs concentrations on the laser-induced heating phenomenon in different media should be studied. In the following work, we studied the maximum dispersion concentration of NPs in solid and fluid matrix. However, the dispersion capacity of $GdVO_4$: Yb^{3+}/Er^{3+} NPs in a sol-gel hybrid glass is not high. Thus, only the PDMS matrix is considered in the following.

Using the same dispersion method, 50 wt.% of $GdVO_4$: Yb^{3+}/Er^{3+} NPs were dispersed in oil and PDMS. When the concentration of NPs is extremely high, the oil suspension and the solid completely lose their transparency. The emission intensity gets higher when the NPs concentration is higher. The high concentrated materials can be excited under low laser power density (1.3 W/cm^2) (Figures S4a and S5a). However, Figures S4b and S5c show that the LIR changes not only with temperature but also with laser intensity, for 50 wt.% in the suspension and in the PDMS respectively, which was observed in a contrasting manner in Figures S2c and S3c.

The temperature calibration curves are plotted in Figure S4c for the NPs suspension, for the 50 wt.% NPs in oil at 2.5 W/cm^2 and for the 0.5 wt.% at 15.8 W/cm^2. The slopes of those two curves are close to each other as well as the calculated ΔE_{LIR}. This observation shows that in the suspension at high concentration of NPs, the laser heating could be overcome under low laser intensity same performance as powder. In Figure S5b, the temperature calibration curves for 50 wt.% of NPs in PDMS at different laser intensities are plotted. The laser heating occurs after 2.5 W/cm^2, the calculated ΔE_{LIR} decreases with the laser intensity. As expected, the materials at high NPs concentration react like NPs powder with respect to the laser heating phenomenon.

As performed for free powder NPs, the equation (5) was applied to correct the laser-induced heating temperature (constant values see SI Table S2) on 50 wt.% NPs in PDMS (Figure S5d). Compared to the regression model fitted for free powder of NPs, their coefficients of I_{laser} (C2), as well as T_{LIR} (C3) are nearly the same. The C2 and C3 are the most crucial coefficients in equation (5). This observation shows that the effect of laser intensity and environmental temperature on laser-induced heating may not depend on dispersed media.

It's important to note that some samples containing a high concentration of NPs were destroyed by laser-induced overheating after the experiments. We observed significant darkening on the surface of high concentrated PDMS after at high laser density excitation. When the laser intensity and temperature are high during calibration, the ambient temperature can easily reach the flash point or melting point of the materials. However, without laser heating calibration, it is difficult to estimate the $T_{laser\ heating}$ on a given I_{laser}. To avoid any unexpectable sample damage, it is necessary to verify the laser heating phenomenon before any experiment using UC nanoparticles as a sensor.

We can conclude that the concentration of $GdVO_4$: Yb^{3+}/Er^{3+} NPs dispersion in the medium has an impact on the laser heating phenomenon. The concentration of the NPs is a critical parameter that decides whether laser heating occurs or not in the studied medium. In our work, laser heating occurs when the NPs concentration is very high (50 wt.%) but not when the concentration is low (0.5 wt.% in a fluid suspension and 5 wt.% in a hybrid glass or PDMS). The laser-induced heating causes the significant temperature calibration error and can even destroy the material. Therefore, when $GdVO_4$: Yb^{3+}/Er^{3+} NPs are used in a medium as thermometric nanoprobes, the phenomenon of laser-induced heating deserves to be studied beforehand. Since laser heating can occur in all UC systems, experiments with UC nanoprobes should pay attention to laser heating. In summary, by using the $GdVO_4$: Yb^{3+}/Er^{3+} NPs as UC nano sensor on temperature measurement, low concentration of NPs in medium or low laser intensity should be used to avoid the error caused by laser-induced heating. To optimize the UC emission, the high concentration of NPs dispersion could be applied only with a laser-induced heating correction.

4. CONCLUSION

A heating effect was observed from a near-infrared laser during the upconversion emission of $GdVO_4$: Yb^{3+}/Er^{3+} nanoparticles powder. This effect became more significant with the increasing laser intensity and the rising ambient temperature. We also studied the photoluminescence properties of $GdVO_4$: Yb^{3+}/Er^{3+} nanoparticles in a dispersed medium, their thermometry was still valid. The laser heating effect could be neglected at low concentration (0.5 wt%/ 5 wt.%) but not at high concentration (50 wt%). To optimize the accuracy of temperature measurement, the $GdVO_4$: Yb^{3+}/Er^{3+} nanoparticles are excited upon high NIR laser intensity with the laser-induced heating temperature correction. With a given laser intensity, the correction may be realized for the NPs on powder form and for the high-concentrated dispersed in solid. The above results show that the laser-induced heating has a crucial impact on accuracy of temperature measurement using UC nano sensor. However, the use of $GdVO_4$: Yb^{3+}/Er^{3+} nanoparticles as temperature sensors will provide a reliable method of measurement as the laser-induced heating can be corrected.

ASSOCIATED CONTENT

Supporting information

Equation S1: Calculation of the intrinsic experimental uncertainty on emission intensity (δI/I)

Table S1: Thermal conductivity of the matrices studied at room temperature (20°C)

Table S2: Constant value in equation of laser-induced heating correction

Figure S1: Peak surface integration for LIR calculation

Figure S2: Suspension at 0.5 wt.% NPs in oil: (a) Emission spectra at different laser intensities. (b) Relationship between the average of the sum of the N1+N2 surface peaks and the laser intensity at studied temperature (25°C to 150°C). (c) LIR at different laser intensities at different setup temperatures (25°C to 150 °C).

Figure S3: Glass at 5 wt.% NPs: (a) Emission spectra at different laser intensities. (b) Relationship between the average of the sum of the N1+N2 surface peaks and the laser intensity at studied temperature (25°C to 160°C). (c) LIR at different laser intensities at different setup temperature (25°C to 160 °C).

Figure S4: Suspension at 50 wt.% NPs in oil: (a) Emission spectra at different laser intensities. (b) LIR at different laser intensities at different setup temperature (25°C to 150 °C). (c) Calibration of the temperature of the suspension to 50 wt.% NPs (blue) at 2.5 W/cm² and at 0.5 wt. % NPs (yellow) at 15.8 W/cm².

Figure S5: PDMS at 50 wt.% NPs: (a) Emission spectra at different laser intensities. (b) Temperature calibration under excitation at 970 nm at different laser intensities. (c) LIR at different laser intensities at different setup temperature (25°C to 160 °C). (d) Application of correction module for laser heating temperature.

AUTHOR INFORMATION

Corresponding Author

*Laurence Bois
Correspondence: laurence.bois@univ-lyon1.fr;
Tel.: +33. 04.72.44.81.66
* David Philippon
Correspondence: david.philippon@insa-lyon.fr;

Author Contributions

C.J. L.B., D.P. and S.D. are the supervisors of projects. Y.Z. and L.B. performed the experiments. G.L., M.M., C.D. and D.F. provided input into the design of the experiments. S.H. wrote the MATLAB code for data analyze. Y.Z., G.L., L.B., D.P. and S.D. co-wrote the manuscript with input from other authors.

Funding Sources

This work was supported by the LABEX MANUTECH-SISE (ANR-10-LABX-0075) of Université de Lyon, within the Plan France 2030 operated by the French National Research Agency (ANR).

ACKNOWLEDGMENT

The authors gratefully acknowledge the Ctμ platform of electronic microscopy (University Lyon 1), Ruben Vera in the "Centre de Diffractométrie Henri Longchambon" (University Lyon 1) and Hervé Pabiou in "CETHIL" (INSA Lyon) for thermal conductivity measurements.

REFERENCES

(1) Childs, P. R. N.; Greenwood, J. R.; Long, C. A. Review of Temperature Measurement. *Rev. Sci. Instrum.* **2000**, *71* (8), 2959–2978. https://doi.org/10.1063/1.1305516.

(2) Quintanilla, M.; Henriksen-Lacey, M.; Renero-Lecuna, C.; Liz-Marzán, L. M. Challenges for Optical Nanothermometry in Biological Environments. *Chem. Soc. Rev.* **2022**, *51* (11), 4223–4242. https://doi.org/10.1039/d2cs00069e.

(3) Van Swieten, T. P.; Van Omme, T.; Van Den Heuvel, D. J.; Vonk, S. J. W.; Spruit, R. G.; Meirer, F.; Garza, H. H. P.; Weckhuysen, B. M.; Meijerink, A.; Rabouw, F. T.; Geitenbeek, R. G. Mapping Elevated Temperatures with a Micrometer Resolution Using the Luminescence of Chemically Stable Upconversion Nanoparticles. *ACS Appl. Nano Mater.* **2021**, *4* (4), 4208–4215. https://doi.org/10.1021/acsanm.1c00657.

(4) Jaque, D.; Vetrone, F. Luminescence Nanothermometry. *Nanoscale* **2012**, *4* (15), 4301–4326. https://doi.org/10.1039/c2nr30764b.

(5) Casar, J. R.; McLellan, C. A.; Siefe, C.; Dionne, J. A. Lanthanide-Based Nanosensors: Refining Nanoparticle Responsiveness for Single Particle Imaging of Stimuli. *ACS Photonics* **2021**, *8* (1), 3–17. https://doi.org/10.1021/acsphotonics.0c00894.

(6) Brites, C. D. S.; Balabhadra, S.; Carlos, L. D. Lanthanide-Based Thermometers: At the Cutting-Edge of Luminescence Thermometry. *Adv. Opt. Mater.* **2019**, *7* (5), 1–30. https://doi.org/10.1002/adom.201801239.

(7) Bednarkiewicz, A.; Marciniak, L.; Carlos, L. D.; Jaque, D. Standardizing Luminescence Nanothermometry for Biomedical Applications. *Nanoscale* **2020**, *12* (27), 14405–14421. https://doi.org/10.1039/d0nr03568h.

(8) Dramićanin, M. D. Sensing Temperature via Downshifting Emissions of Lanthanide-Doped Metal Oxides and Salts. A Review. *Methods Appl. Fluoresc.* **2016**, *4* (4). https://doi.org/10.1088/2050-6120/4/4/042001.

(9) Dramićanin, M. D. Trends in Luminescence Thermometry. *J. Appl. Phys.* **2020**, *128* (4). https://doi.org/10.1063/5.0014825.

(10) Han, B.; Hanson, W. L.; Bensalah, K.; Tuncel, A.; Stern, J. M.; Cadeddu, J. A. Development of Quantum Dot-Mediated Fluorescence Thermometry for Thermal Therapies. *Ann. Biomed. Eng.* **2009**, *37* (6), 1230–1239. https://doi.org/10.1007/s10439-009-9681-6.

(11) Albahrani, S. M. B.; Seoudi, T.; Philippon, D.; Lafarge, L.; Reiss, P.; Hajjaji, H.; Guillot, G.; Querry, M.; Bluet, J. M.; Vergne, P. Quantum Dots to Probe Temperature and Pressure in Highly Confined Liquids. *RSC Adv.* **2018**, *8* (41), 22897–22908. https://doi.org/10.1039/C8RA03652G.

(12) Seoudi, T.; Philippon, D.; Fillot, N.; Lafarge, L.; Devaux, N.; Mondelin, A.; Vergne, P. CdSe-Based Quantum Dots as In Situ Pressure and Temperature Non-Intrusive Sensors in Elastohydrodynamic Contacts. *Tribol. Lett.* **2020**, *68* (3). https://doi.org/10.1007/s11249-020-01312-x.

(13) Homeyer, E.; Pailhès, S.; Debord, R.; Jary, V.; Dujardin, C.; Ledoux, G. Diamond Contact-Less Micrometric Temperature Sensors. *Appl. Phys. Lett.* **2015**, *106* (24). https://doi.org/10.1063/1.4921177.

(14) Wade, S. A.; Collins, S. F.; Baxter, G. W. Fluorescence Intensity Ratio Technique for Optical Fiber Point Temperature Sensing. *J. Appl. Phys.* **2003**, *94* (8), 4743–4756. https://doi.org/10.1063/1.1606526.

(15) Runowski, M.; Shyichuk, A.; Tymiński, A.; Grzyb, T.; Lavín, V.; Lis, S. Multifunctional Optical Sensors for Nanomanometry and Nanothermometry: High-Pressure and High-Temperature Upconversion Luminescence of Lanthanide-Doped Phosphates - LaPO4/YPO4:Yb3+-Tm3+. *ACS Appl. Mater. Interfaces* **2018**, *10* (20), 17269–17279. https://doi.org/10.1021/acsami.8b02853.

(16) Cheng, Y.; Gao, Y.; Lin, H.; Huang, F.; Wang, Y. Strategy Design for Ratiometric Luminescence Thermometry: Circumventing the Limitation of Thermally Coupled Levels. *J. Mater. Chem. C* **2018**, *6* (28), 7462–7478. https://doi.org/10.1039/c8tc02401d.

(17) Ansari, A. A.; Parchur, A. K.; Nazeeruddin, M. K.; Tavakoli, M. M. Luminescent Lanthanide Nanocomposites in Thermometry: Chemistry of Dopant Ions and Host Matrices. *Coord. Chem. Rev.* **2021**, *444*, 214040. https://doi.org/10.1016/j.ccr.2021.214040.

(18) Bhiri, N. M.; Dammak, M.; Aguiló, M.; Díaz, F.; Carvajal, J. J.; Pujol, M. C. Stokes and Anti-Stokes Operating Conditions Dependent Luminescence Thermometric Performance of Er3+-Doped and Er3+, Yb3+ Co-Doped GdVO4 Microparticles in the Non-Saturation Regime. *J. Alloys Compd.* **2020**, *814*. https://doi.org/10.1016/j.jallcom.2019.152197.

(19) Lee, C.; Xu, E. Z.; Liu, Y.; Teitelboim, A.; Yao, K.; Fernandez-Bravo, A.; Kotulska, A. M.; Nam, S. H.; Suh, Y. D.; Bednarkiewicz, A.; Cohen, B. E.; Chan, E. M.; Schuck, P. J. Giant Nonlinear Optical Responses from Photon-Avalanching Nanoparticles. *Nature* **2021**, *589* (7841), 230–235. https://doi.org/10.1038/s41586-020-03092-9.

(20) Chen, Y.; Mishra, S.; Ledoux, G.; Jeanneau, E.; Daniel, M.; Zhang, J.; Daniele, S. Direct Synthesis of Hexagonal NaGdF4 Nanocrystals from a Single-Source Precursor: Upconverting NaGdF4:Yb3+,Tm 3+ and Its Composites with TiO2 for near-IR-Driven Photocatalysis. *Chem. - An Asian J.* **2014**, *9* (9), 2415–2421. https://doi.org/10.1002/asia.201402347.

(21) Li, X.; Yang, C.; Yu, Y.; Li, Z.; Lin, J.; Guan, X.; Zheng, Z.; Chen, D. Dual-Modal Photon Upconverting and Downshifting Emissions from Ultra-Stable CsPbBr3Perovskite Nanocrystals Triggered by Co-Growth of Tm:NaYbF4Nanocrystals in Glass. *ACS Appl. Mater. Interfaces* **2020**, *12* (16), 18705–18714. https://doi.org/10.1021/acsami.0c01968.

(22) Marciniak, L.; Waszniewska, K.; Bednarkiewicz, A.; Hreniak, D.; Strek, W. Sensitivity of a Nanocrystalline Luminescent Thermometer in High and Low Excitation Density Regimes. *J. Phys. Chem. C* **2016**, *120* (16), 8877–8882. https://doi.org/10.1021/acs.jpcc.6b01636.

(23) Cui, Y.; Zheng, L.; Xu, W.; Liu, H.; Li, L.; Zhang, Z. Influence of 980 Nm Pump Power on Optical Thermometry Based on NaYF4:Yb3+/Er3+ Nanoparticles. *Mater. Res. Express* **2018**, *5* (6). https://doi.org/10.1088/2053-1591/aac6fd.

(24) Antoniak, M. A.; Zelewski, S. J.; Oliva, R.; Żak, A.; Kudrawiec, R.; Nyk, M. Combined Temperature and Pressure Sensing Using Luminescent NaBiF4:Yb,Er Nanoparticles. *ACS Appl. Nano Mater.* **2020**, *3* (5), 4209–4217. https://doi.org/10.1021/acsanm.0c00403.

(25) Ding, M.; Lu, C.; Chen, L.; Bai, W.; Yuan, Y.; Ji, Z. Transparent Sol-Gel Glass Ceramics Containing β-NaYF4:Yb3+/Er3+ Nanocrystals: Structure, Upconversion Luminescent Properties and Optical Thermometry Behavior. *Ceram. Int.* **2018**, *44* (14), 16379–16387. https://doi.org/10.1016/j.ceramint.2018.06.047.

(26) Zhang, F.; Li, G.; Zhang, W.; Yan, Y. L. Phase-Dependent Enhancement of the Green-Emitting Upconversion Fluorescence in LaVO4:Yb3+, Er3+. *Inorg. Chem.* **2015**, *54* (15), 7325–7334. https://doi.org/10.1021/acs.inorgchem.5b00851.

(27) Cui, X.; Cheng, Y.; Lin, H.; Huang, F.; Wu, Q.; Wang, Y. Size-Dependent Abnormal Thermo-Enhanced Luminescence of Ytterbium-Doped Nanoparticles. *Nanoscale* **2017**, *9* (36), 13794–13799. https://doi.org/10.1039/c7nr04575a.

(28) Artur Tymiński, T. G. Are Rare Earth Phosphates Suitable as Hosts for Upconversion Luminescence? Studies on Nanocrystalline REPO4 (RE = Y, La, Gd, Lu) Doped with Yb 3+/Ho 3+, Yb 3+/Er3+, Yb 3+/Tm3+, Yb 3+/Tb 3+ and Yb 3+/Tb 3+/Eu 3+ Ions. *J. Lumin.* **2017**, *181*, 411–420. https://doi.org/doi.org/10.1016/j.jlumin.2016.09.028.

(29) Ćirić, A.; Gavrilović, T.; Dramićanin, M. D. Luminescence Intensity Ratio Thermometry with Er3+: Performance Overview. *Crystals* **2021**, *11* (2), 1–19. https://doi.org/10.3390/cryst11020189.

(30) Goderski, S.; Runowski, M.; Woźny, P.; Lavín, V.; Lis, S. Lanthanide Upconverted Luminescence for Simultaneous Contactless Optical Thermometry and Manometry-Sensing under Extreme Conditions of Pressure and Temperature. *ACS Appl. Mater. Interfaces* **2020**, *12* (36), 40475–40485. https://doi.org/10.1021/acsami.0c09882.

(31) Runowski, M.; Stopikowska, N.; Szeremeta, D.; Goderski, S.; Skwierczyńska, M.; Lis, S. Upconverting Lanthanide Fluoride Core@Shell Nanorods for Luminescent Thermometry in the First and Second Biological Windows: β-NaYF 4 :Yb 3+ - Er 3+ @SiO 2 Temperature Sensor. *ACS Appl. Mater. Interfaces* **2019**, *11* (14), 13389–13396. https://doi.org/10.1021/acsami.9b00445.

(32) Auzel, F. Upconversion and Anti-Stokes Processes with f and d Ions in Solids. *Chem. Rev.* **2004**, *104* (1), 139–173. https://doi.org/10.1021/cr020357g.

(33) Himmelstoß, S. F.; Hirsch, T. A Critical Comparison of Lanthanide Based Upconversion Nanoparticles to Fluorescent Proteins, Semiconductor Quantum Dots, and Carbon Dots for Use in Optical Sensing and Imaging. *Methods Appl. Fluoresc.* **2019**, *7* (2). https://doi.org/10.1088/2050-6120/ab0bfa.

(34) Chen, B.; Wang, F. Combating Concentration Quenching in Upconversion Nanoparticles. *Acc. Chem. Res.* **2019**. https://doi.org/10.1021/acs.accounts.9b00453.

(35) Wang, F.; Wang, J.; Liu, X. Direct Evidence of a Surface Quenching Effect on Size-Dependent Luminescence of Upconversion Nanoparticles. *Angew. Chemie - Int. Ed.* **2010**, *49* (41), 7456–7460. https://doi.org/10.1002/anie.201003959.

(36) Zhao, J.; Li, H.; Zeng, Q.; Song, K.; Wang, X.; Kong, X. Temperature-Dependent Upconversion Luminescence of NaYF 4 :Yb 3+ ,Er 3+ Nanoparticles . *Chem. Lett.* **2013**, *42* (3), 310–312. https://doi.org/10.1246/cl.2013.310.

(37) Yingchao Yan; Anne Jans Faber; Waal, H. de. Luminescence Quenching by OH Groups in Highly Er-Dopedphosphate Glasses. *J. Non. Cryst. Solids* **1995**, *181*, 283–290.

(38) Wang, H.; Yin, X.; Xing, M.; Fu, Y.; Tian, Y.; Feng, X.; Jiang, T.; Luo, X. Thermal Effects of Er3+/Yb3+-Doped NaYF4 Phosphor Induced by 980/1510 Nm Laser Diode Irradiation. *J. Am. Ceram. Soc.* **2018**, *101* (2), 865–873. https://doi.org/10.1111/jace.15246.

(39) Joseph, R. E.; Busko, D.; Hudry, D.; Gao, G.; Biner, D.; Krämer, K.; Turshatov, A.; Richards, B. S.; Howard, I. A. A Method for Correcting the Excitation Power Density Dependence of Upconversion Emission Due to Laser-Induced Heating. *Opt. Mater. (Amst).* **2018**, *82* (February), 65–70. https://doi.org/10.1016/j.optmat.2018.05.025.

(40) Zhang, W. W.; Gao, Y. Q.; He, X. D.; Li, S. Monitoring of Laser Heating Temperature in Laser Spectroscopic Measurements. *Opt. Commun.* **2012**, *285* (9), 2414–2417. https://doi.org/10.1016/j.optcom.2012.01.009.

(41) Dey, R.; Pandey, A.; Rai, V. K. Er3+-Yb3+ and Eu3+-Er3+-Yb 3+ Codoped Y2O3 Phosphors as Optical Heater. *Sensors Actuators, B Chem.* **2014**, *190*, 512–515. https://doi.org/10.1016/j.snb.2013.09.025.

(42) Tikhomirov, V. K.; Driesen, K.; Rodriguez, V. D.; Gredin, P.; Mortier, M. Optical Nanoheater Based on the Yb3+-Er3+ Co- Doped Nanoparticles V.K. *Opt. Express* **2009**, *17* (14), 11794–11798.

(43) Zhang, Z.; Suo, H.; Zhao, X.; Sun, D.; Fan, L.; Guo, C. NIR-to-NIR Deep Penetrating Nanoplatforms Y2O3:Nd3+/Yb3+@SiO2@Cu2S toward Highly Efficient Photothermal Ablation. *ACS Appl. Mater. Interfaces* **2018**, *10* (17), 14570–14576. https://doi.org/10.1021/acsami.8b03239.

(44) Sun, J.; Zhang, Z.; Suo, H.; Chen, Y.; Xiang, J.; Guo, C. Temperature Self-Monitoring Photothermal Nano-Particles of Er3+/Yb3+ Co-Doped Zircon-Tetragonal BiVO4. *Ceram. Int.* **2021**, *47* (1), 409–415. https://doi.org/10.1016/j.ceramint.2020.08.147.

(45) Carrasco, E.; Del Rosal, B.; Sanz-Rodríguez, F.; De La Fuente, Á. J.; Gonzalez, P. H.; Rocha, U.; Kumar, K. U.; Jacinto, C.; Solé, J. G.; Jaque, D. Intratumoral Thermal Reading during Photo-Thermal Therapy by Multifunctional Fluorescent Nanoparticles. *Adv. Funct. Mater.* **2015**, *25* (4), 615–626. https://doi.org/10.1002/adfm.201403653.

(46) Purohit, B.; Amans, D.; Guyot, Y.; Mahler, B.; Joubert, M. F.; Dujardin, C.; Daniele, S.; Ledoux, G.; Mishra, S. Quest to Enhance Up-Conversion Efficiency: A Comparison of Anhydrous vs. Hydrous Synthesis of NaGdF4: Yb3+ and Tm3+ Nanoparticles. *Mater. Today Chem.* **2020**, *17*. https://doi.org/10.1016/j.mtchem.2020.100326.

(47) Suo, H.; Zhao, X.; Zhang, Z.; Li, T.; Goldys, E. M.; Guo, C. Constructing Multiform Morphologies of YF: Er3+/Yb3+up-Conversion Nano/Micro-

Crystals towards Sub-Tissue Thermometry. *Chem. Eng. J.* **2017**, *313*, 65–73. https://doi.org/10.1016/j.cej.2016.12.064.
(48) Zhu, J.; Wang, S.; Yang, Z.; Liao, S.; Lin, J.; Yao, H.; Huang, F.; Zheng, Y.; Chen, D. A Single-Beam NIR Laser-Triggered Full-Color Upconversion Tuning of a Er/Tm:CsYb2F7@glass Photothermal Nanocomposite for Optical Security. **2022**, 3407–3415. https://doi.org/10.1039/d1nr08535b.
(49) Wang, S.; Lin, J.; Li, X.; Chen, J.; Yang, C.; Huang, P.; Cheng, Y.; Chen, D. Glass-Limited Yb/Er:NaLuF4nanocrystals: Reversible Hexagonal-to-Cubic Phase Transition and Anti-Counterfeiting. *J. Mater. Chem. C* **2020**, *8* (45), 16151–16159. https://doi.org/10.1039/d0tc03775c.
(50) Wang, S.; Lin, J.; He, Y.; Chen, J.; Yang, C.; Huang, F.; Chen, D. Remarkable Laser-Driven Upconverting Photothermal Effect of Cs3LnF6@glass Nanocomposites for Anti-Counterfeiting. *Chem. Eng. J.* **2020**, *394* (January), 124889. https://doi.org/10.1016/j.cej.2020.124889.
(51) Erol, E.; Kibrisli, O.; Vahedigharehchopogh, N.; Çelikbilek Ersundu, M.; Ersundu, A. E. The Synergistic Effect of Er3+and Ho3+on Temporal Color Tuning of Upconversion Emission in a Glass Host: Via a Facile Excitation Modulation Technique for Anti-Counterfeiting Applications. *Phys. Chem. Chem. Phys.* **2020**, *22* (44), 25963–25972. https://doi.org/10.1039/d0cp04809g.
(52) Bednarkiewicz, A.; Wawrzynczyk, D.; Gagor, A.; Kepinski, L.; Kurnatowska, M.; Krajczyk, L.; Nyk, M.; Samoc, M.; Strek, W. Giant Enhancement of Upconversion in Ultra-Small Er 3+/Yb 3+:NaYF 4 Nanoparticles via Laser Annealing. *Nanotechnology* **2012**, *23* (14). https://doi.org/10.1088/0957-4484/23/14/145705.
(53) Wawrzynczyk, D.; Bednarkiewicz, A.; Nyk, M.; Strek, W.; Samoc, M. Neodymium(Iii) Doped Fluoride Nanoparticles as Non-Contact Optical Temperature Sensors. *Nanoscale* **2012**, *4* (22), 6959–6961. https://doi.org/10.1039/c2nr32203j.
(54) Debasu, M. L.; Ananias, D.; Pastoriza-Santos, I.; Liz-Marzán, L. M.; Rocha, J.; Carlos, L. D. All-in-One Optical Heater-Thermometer Nanoplatform Operative from 300 to 2000 K Based on Er3+ Emission and Blackbody Radiation. *Adv. Mater.* **2013**, *25* (35), 4868–4874. https://doi.org/10.1002/adma.201300892.
(55) Piñol, R.; Brites, C. D. S.; Bustamante, R.; Martínez, A.; Silva, N. J. O.; Murillo, J. L.; Cases, R.; Carrey, J.; Estepa, C.; Sosa, C.; Palacio, F.; Carlos, L. D.; Millán, A. Joining Time-Resolved Thermometry and Magnetic-Induced Heating in a Single Nanoparticle Unveils Intriguing Thermal Properties. *ACS Nano* **2015**, *9* (3), 3134–3142. https://doi.org/10.1021/acsnano.5b00059.
(56) Du, P.; Luo, L.; Huang, X.; Yu, J. S. Ultrafast Synthesis of Bifunctional Er 3+ /Yb 3+ -Codoped NaBiF 4 Upconverting Nanoparticles for Nanothermometer and Optical Heater. *J. Colloid Interface Sci.* **2018**, *514*, 172–181. https://doi.org/10.1016/j.jcis.2017.12.027.
(57) Suo, H.; Zhao, X.; Zhang, Z.; Guo, C. 808 Nm Light-Triggered Thermometer-Heater Upconverting Platform Based on Nd3+-Sensitized Yolk-Shell GdOF@SiO2. *ACS Appl. Mater. Interfaces* **2017**, *9* (50), 43438–43448. https://doi.org/10.1021/acsami.7b12753.
(58) Wei, Y.; Su, C.; Zhang, H.; Shao, J.; Fu, Z. Thermal Sensor and Optical Heater of Upconversion Phosphor: Yb3+/Er3+ Co-Doped KY(MoO4)2. *Phys. B Condens. Matter* **2017**, *525* (May), 149–153. https://doi.org/10.1016/j.physb.2017.06.046.
(59) Savchuk, O. A.; Carvajal, J. J.; Brites, C. D. S.; Carlos, L. D.; Aguilo, M.; Diaz, F. Upconversion Thermometry: A New Tool to Measure the Thermal Resistance of Nanoparticles. *Nanoscale* **2018**, *10* (14), 6602–6610. https://doi.org/10.1039/c7nr08758f.
(60) Mahata, M. K.; Kumar, K.; Rai, V. K. Er3+–Yb3+ Doped Vanadate Nanocrystals: A Highly Sensitive Thermographic Phosphor and Its Optical Nanoheater Behavior. *Sensors Actuators B Chem.* **2015**, *209*, 775–780. https://doi.org/10.1016/j.snb.2014.12.039.
(61) Suo, H.; Zhao, X.; Zhang, Z.; Wu, Y.; Guo, C. Upconverting LuVO4:Nd3+/Yb3+/Er3+@SiO2@Cu2S Hollow Nanoplatforms for Self-Monitored Photothermal Ablation. *ACS Appl. Mater. Interfaces* **2018**, *10* (46), 39912–39920. https://doi.org/10.1021/acsami.8b18184.
(62) Deng, R.; Qin, F.; Chen, R.; Huang, W.; Hong, M.; Liu, X. Temporal Full-Colour Tuning through Non-Steady-State Upconversion. *Nat. Nanotechnol.* **2015**, *10* (3), 237–242. https://doi.org/10.1038/nnano.2014.317.
(63) Bettinelli, M. Upconversion Nanocrystals: Bright Colours Ahead. *Nat. Nanotechnol.* **2015**, *10* (3), 203–204. https://doi.org/10.1038/nnano.2015.31.
(64) Han, Y.; Li, H.; Wang, Y.; Pan, Y.; Huang, L.; Song, F.; Huang, W. Upconversion Modulation through Pulsed Laser Excitation for Anti-Counterfeiting. *Sci. Rep.* **2017**, *7* (1), 1–8. https://doi.org/10.1038/s41598-017-01611-9.
(65) Xia, X.; Volpi, A.; Roh, J. Y. D.; De Siena, M. C.; Gamelin, D. R.; Hehlen, M. P.; Pauzauskie, P. J. The Impact of 2H9/2 → 4I13/2 Emission from Er3+ Ions on Ratiometric Optical Temperature Sensing with Yb3+/Er3+ Co-Doped Upconversion Materials. *J. Lumin.* **2021**, *236* (December 2020), 118006. https://doi.org/10.1016/j.jlumin.2021.118006.
(66) Martins, J. C.; Bastos, A. R. N.; Ferreira, R. A. S.; Wang, X.; Chen, G.; Carlos, L. D. Primary Luminescent Nanothermometers for Temperature Measurements Reliability Assessment. *Adv. Photonics Res.* **2021**, *2* (5), 2000169. https://doi.org/10.1002/adpr.202000169.
(67) Dwivedi, A.; Kumar, D.; Rai, S. B.; Rai, A. K. Effect of Host on the Radiative (Upconversion Emission) as Well as Non-Radiative Relaxation (Laser Induced Optical Heating) in Tm3+/Yb3+ Co-Doped Phosphors. *J. Lumin.* **2020**, *226* (June), 117421. https://doi.org/10.1016/j.jlumin.2020.117421.
(68) Paz-Buclatin, F.; Rivera-López, F.; González, O.; Martín, I. R.; Martin, L. L.; Jovanović, D. J. GdVO4:Er3+/Yb3+ Nanocrystalline Powder as Fluorescence Temperature Sensor. Application to Monitor the Temperature of an Electrical Component. *Sensors Actuators, A Phys.* **2019**, *299*. https://doi.org/10.1016/j.sna.2019.111628.
(69) Chateau, D.; Chaput, F.; Lopes, C.; Lindgren, M.; Brännlund, C.; Öhgren, J.; Djourelov, N.; Nedelec, P.; Desroches, C.; Eliasson, B.; Kindahl, T.; Lerouge, F.; Andraud, C.; Parola, S. Silica Hybrid Sol-Gel Materials with Unusually High Concentration of Ptorganic Molecular Guests: Studies of Luminescence and Nonlinear Absorption of Light. *ACS Appl. Mater. Interfaces* **2012**, *4* (5), 2369–2377. https://doi.org/10.1021/am2015537.
(70) Rakov, N.; Maciel, G. S.; Xiao, M. Upconversion Fluorescence and Its Thermometric Sensitivity of Er3+:Yb3+ Co-Doped SrF2 Powders Prepared by Combustion Synthesis. *Electron. Mater. Lett.* **2014**, *10* (5), 985–989. https://doi.org/10.1007/s13391-014-4030-9.
(71) Brites, C. D. S.; Millán, A.; Carlos, L. D. *Lanthanides in Luminescent Thermometry*; 2016; Vol. 49. https://doi.org/10.1016/bs.hpcre.2016.03.005.
(72) Li, L.; Qin, F.; Zhou, Y.; Zheng, Y.; Zhao, H.; Zhang, Z. Approximate Energy Gaps, Dissimilar Relative Thermal Sensitivities. *Sensors Actuators, B Chem.* **2018**, *269*, 203–209. https://doi.org/10.1016/j.snb.2018.04.158.
(73) Perrella, R. V.; De Sousa Filho, P. C. High-Sensitivity Dual UV/NIR-Excited Luminescence Thermometry by Rare Earth Vanadate Nanoparticles. *Dalt. Trans.* **2020**, *49* (3), 911–922. https://doi.org/10.1039/c9dt04308j.
(74) Huignard, A.; Buissette, V.; Laurent, G.; Gacoin, T.; Boilot, J. P. Synthesis and Characterizations of YVO4: Eu Colloids. *Chem. Mater.* **2002**, *14* (5), 2264–2269. https://doi.org/10.1021/cm011263a.
(75) Alkahtani, M.; Alfahd, A.; Alsofyani, N.; Almuqhim, A. A.; Qassem, H.; Alshehri, A. A.; Almughem, F. A.; Hemmer, P. Photostable and Small Yvo4:Yb,Er Upconversion Nanoparticles in Water. *Nanomaterials* **2021**, *11* (6). https://doi.org/10.3390/nano11061535.
(76) Liu, L.; Yue, S.; Zhang, Y.; Qin, R.; Liu, L.; Zhang, D.; Sun, R.; Chen, L. One-Pot Reverse Microemulsion Synthesis of Core-Shell Structured YVO4:Eu3+@SiO2 Nanocomposites. *Opt. Mater. (Amst).* **2015**, *39* (3), 207–210. https://doi.org/10.1016/j.optmat.2014.11.027.
(77) Yang, L.; Peng, S.; Zhao, M.; Yu, L. New Synthetic Strategies for Luminescent YVO 4 :Ln 3+ (Ln = Pr, Sm, Eu, Tb, Dy, Ho, Er) with Mesoporous Cell-like Nanostructure . *Opt. Mater. Express* **2018**, *8* (12), 3805. https://doi.org/10.1364/ome.8.003805.
(78) Liu, J.; Deng, H.; Huang, Z.; Zhang, Y.; Chen, D.; Shao, Y. Phonon-Assisted Energy Back Transfer-Induced Multicolor Upconversion Emission of Gd2O3:Yb3+/Er3+ Nanoparticles under near-Infrared Excitation. *Phys. Chem. Chem. Phys.* **2015**, *17* (23), 15412–15418.

https://doi.org/10.1039/c5cp01632k.
(79) Savchuk, O. A.; Carvajal, J. J.; Massons, J.; Cascales, C.; Aguiló, M.; Díaz, F. Novel Low-Cost, Compact and Fast Signal Processing Sensor for Ratiometric Luminescent Nanothermometry. *Sensors Actuators, A Phys.* **2016**, *250*, 87–95. https://doi.org/10.1016/j.sna.2016.08.031.
(80) Sedlmeier, A.; Achatz, D. E.; Fischer, L. H.; Gorris, H. H.; Wolfbeis, O. S. Photon Upconverting Nanoparticles for Luminescent Sensing of Temperature. *Nanoscale* **2012**, *4* (22), 7090–7096. https://doi.org/10.1039/c2nr32314a.
(81) Wujczyk, M.; Watras, A.; Szyszka, K.; Wiglusz, R. J. Influence of Vanadium Concentration on Up-Conversion Luminescence in Er3+–Yb3+ and Tm3+–Yb3+ Ions Pair Co-Doped YVxP1−xO4 Solid State Solution. *J. Alloys Compd.* **2021**, *884*, 161022. https://doi.org/10.1016/j.jallcom.2021.161022.
(82) Buissette, V.; Huignard, A.; Gacoin, T.; Boilot, J. P.; Aschehoug, P.; Viana, B. Luminescence Properties of YVO4:Ln (Ln = Nd, Yb, and Yb-Er) Nanoparticles. *Surf. Sci.* **2003**, *532–535*, 444–449. https://doi.org/10.1016/S0039-6028(03)00203-6.
(83) Cho, Y.; Song, S. W.; Lim, S. Y.; Kim, J. H.; Park, C. R.; Kim, H. M. Spectral Evidence for Multi-Pathway Contribution to the Upconversion Pathway in NaYF4:Yb3+,Er3+ Phosphors. *Phys. Chem. Chem. Phys.* **2017**, *19* (10), 7326–7332. https://doi.org/10.1039/c7cp00048k.
(84) Li, T.; Guo, C.; Li, L. Up-Conversion Luminescence of Er^3+-Yb^3+ Co-Doped CaIn_2O_4. *Opt. Express* **2013**, *21* (15), 18281. https://doi.org/10.1364/oe.21.018281.
(85) Oh, J. H.; Moon, B. K.; Choi, B. C.; Jeong, J. H.; Choi, H.; Kim, J. H. Reinterpretation of the Red Emission Pathway in β-NaYF4:Yb3+, Er3+. *Ceram. Int.* **2017**, *43* (2), 2517–2522. https://doi.org/10.1016/j.ceramint.2016.11.053.
(86) Rühl, P.; Wang, D.; Garwe, F.; Müller, R.; Haase, M.; Krämer, K. W.; Paa, W.; Heintzmann, R.; Heinemann, S. H.; Stafast, H. Notes on Thermometric Artefacts by Er3+ Luminescence Band Interference. *J. Lumin.* **2021**, *232* (December 2020), 18–21. https://doi.org/10.1016/j.jlumin.2020.117860.
(87) Suo, H.; Zhao, X.; Zhang, Z.; Guo, C. Ultra-Sensitive Optical Nano-Thermometer LaPO4: Yb3+/Nd3+ Based on Thermo-Enhanced NIR-to-NIR Emissions. *Chem. Eng. J.* **2020**, *389* (February), 124506. https://doi.org/10.1016/j.cej.2020.124506.
(88) Xu, S.; Xiang, S.; Zhang, Y.; Zhang, J.; Li, X.; Sun, J.; Cheng, L.; Chen, B. 808 Nm Laser Induced Photothermal Effect on Sm3+/Nd3+ Doped NaY(WO4)2 Microstructures. *Sensors Actuators, B Chem.* **2017**, *240*, 386–391. https://doi.org/10.1016/j.snb.2016.08.176.
(89) Riseberg, L. A.; Moos, H. W. Multiphonon Orbit-Lattice Relaxation of Excited States of Rare-Earth Ions in Crystals. *Phys. Rev.* **1968**, *174* (2), 429–438. https://doi.org/10.1103/PhysRev.174.429.
(90) Gavrilović, T. V.; Jovanović, D. J.; Lojpur, V.; Dramićanin, M. D. Multifunctional Eu3+- and Er3+/Yb3+-Doped GdVO4 Nanoparticles Synthesized by Reverse Micelle Method. *Sci. Rep.* **2014**, *4*, 1–9. https://doi.org/10.1038/srep04209.

Laser-induced heating in $GdVO_4$: Yb^{3+}/Er^{3+} nanocrystals for thermometry (For Table of Contents Only)